

Transient Density-Induced Dipolar Interactions in a Thin Vapor Cell

Florian Christaller,¹ Max Mäusezahl,¹ Felix Moutmsilis,¹ Annika Belz,^{1,2} Harald Kübler,¹ Hadiseh Alaeian,³ Charles S. Adams,² Robert Löw,¹ and Tilman Pfau^{1,*}

¹*Physikalisches Institut and Center for Integrated Quantum Science and Technology, Universität Stuttgart, Pfaffenwaldring 57, 70569 Stuttgart, Germany*

²*Department of Physics, Joint Quantum Centre (JQC) Durham-Newcastle, Durham University, South Road, Durham, DH1 3LE, United Kingdom*

³*Elmore Family School of Electrical and Computer Engineering, Department of Physics and Astronomy, Purdue Quantum Science and Engineering Institute, Purdue University, West Lafayette, Indiana 47907, USA*

(Dated: April 29, 2022)

We exploit the effect of light-induced atomic desorption to produce high atomic densities ($n \gg k^3$) in a rubidium vapor cell. An intense off-resonant laser is pulsed for roughly one nanosecond on a micrometer-sized sapphire-coated cell, which results in the desorption of atomic clouds from both internal surfaces. We probe the transient atomic density evolution by time-resolved absorption spectroscopy. With a temporal resolution of ≈ 1 ns, we measure the broadening and line shift of the atomic resonances. Both broadening and line shift are attributed to dipole-dipole interactions. This fast switching of the atomic density and dipolar interactions could be the basis for future quantum devices based on the excitation blockade.

The effect of dipole-dipole interactions in optical media becomes important when the density n is significantly larger than the wave number cubed k^3 of the interaction light field. Entering this regime leads to interesting nonlinear effects such as an excitation blockade [1], non-classical photon scattering [2], self-broadening (collisional broadening) [3], and the collective Lamb shift [4, 5].

Dipole-dipole interactions are observable in steady-state experiments performed in thin alkali vapor cells [6–8], where the cells are heated to temperatures above 300 °C. Dipolar broadening effects were previously observed to be independent of the system geometry, while the line shift depends on the dimensionality of the system, as investigated in a 2D model [8, 9]. It is however not straightforward to prepare high densities with alkali vapors [10].

One technique to increase the atomic density is light-induced atomic desorption (LIAD) [11–16] or light-activated dispensers [17]. LIAD is commonly used for loading magneto-optical traps [18–20] and has been studied in confined geometries like photonic-band gap fibers [21, 22] or porous samples [23]. However, the application of pulsed LIAD for fast switching of dipole-dipole interactions is so far unexplored.

In our pulsed LIAD setup, we can switch the atomic density in the nanosecond domain, which allows one to study the dipole-dipole interaction on a timescale faster than the natural atomic lifetime. This fast density switching has been already used in our group to realize an on-demand room-temperature single-photon source based on the Rydberg blockade [24]. In this work, we study the dipolar interaction for the two transitions D_1 : $5S_{1/2} \rightarrow 5P_{1/2}$ and D_2 : $5S_{1/2} \rightarrow 5P_{3/2}$ of rubidium with different transition dipole moments.

We first describe our LIAD measurement results in a thicker part of the cell [cell thickness $L = 6.24(7)$ μm]

at a low density ($nk^{-3} \approx 1$). This measurement is used as the basis to set up a model for the velocity and density distribution of the desorbed atoms. Then, we focus on a thinner part of the cell [$L = 0.78(2)$ μm], where we can study transient density-dependent dipolar interactions at a high density (up to $nk^{-3} \approx 100$). To this end, we compare two transitions (D_1 and D_2 transition of rubidium) with different transition dipole moments to investigate their influences on the dipole-dipole interaction in a quasi-2D geometry ($L \approx \lambda_{\text{probe}}$).

We use a self-made, wedge-shaped, micrometer-sized cell with an attached reservoir tube filled with rubidium (72% ^{85}Rb , 28% ^{87}Rb), shown in Fig. 1(b). By heating the cell independently from the reservoir, we can produce a certain rubidium coverage on the cell walls and a vapor pressure in the cell with a comparably small background density $n \approx 10^{14}$ cm^{-3} (reservoir temperature $T_{\text{res}} \approx 180$ °C). In our setup, the pulsed LIAD laser and the probe laser are aligned collinearly in front of the cell [Fig. 1(a)]. The pulsed LIAD laser at 532 nm has a pulse length of 1.1(1) ns (FWHM) and a repetition rate of 50 kHz. This off-resonant pulse leads to the desorption of rubidium atoms bound to the sapphire-coated glass surface. The amount of desorbed atoms depends on the peak intensity I of the LIAD pulse. We probe the desorbed atoms at 795 nm (D_1 transition of Rb) or 780 nm (D_2 transition of Rb). Both probe lasers have an intensity well below the resonant D_2 saturation intensity $I_{\text{probe}} < 0.01 I_{\text{sat}, D_2}$. The measured Gaussian beam waist radius ($1/e^2$) of the probe laser is $w_{\text{probe}} = 2.0(2)$ μm , while the LIAD laser has a waist radius of $w_{\text{LIAD}} = 13.7(1)$ μm . We measure the transmitted photons with a single-photon counting module, which is read out by a time tagger module. Our wedge-shaped cell has a point of contact of the cell walls, which can be seen

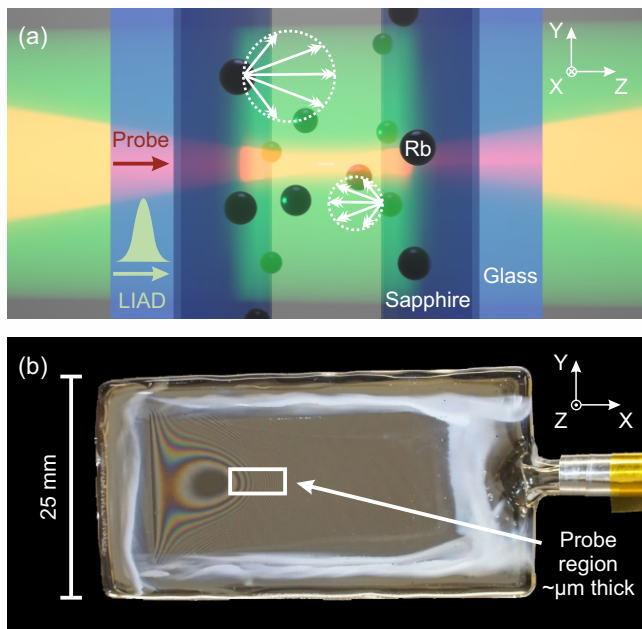


FIG. 1. (a) Illustration of the LIAD process. A green laser pulse (LIAD pulse) desorbs rubidium (Rb) atoms, which are adsorbed on the inner, sapphire-coated surface of the glass cell. The desorbed atoms are emitted with a certain velocity distribution into the cell volume from both sides of the cell, where they are probed with a red laser (probe laser). (b) Photo of the wedge-shaped micrometer-sized cell with interference fringes (Newton's rings). The cell thickness in the probe region is determined interferometrically and ranges from $0.78(2)$ to $6.24(7)$ μm from left to right.

in Fig. 1(b) as a dark circle. To the right of this point lies the probe region where the cell is less than 10 μm thick. The local cell thickness can be directly determined interferometrically by counting Newton's rings.

During the measurement, the probe laser is scanned over the D_1 or D_2 transition at a slow frequency of 11 Hz. At the same time, the LIAD laser sends pulses with a high repetition rate (50 kHz) into the cell. We take full scans of the probe detuning δ at different times t after the LIAD pulse (see Supplemental Material [25]). The time-resolved transmission $T(t, \delta)$ of the probe laser is used to calculate the change of the optical depth ΔOD . For every detuning, the transmission before the LIAD pulse is used as the background signal $T_0(t < 0, \delta)$, which is used to calculate $\Delta\text{OD}(t, \delta) = \ln(T_0/T)$. Thereby the optical depth caused by the background vapor pressure is subtracted. A map of the time- and detuning-resolved ΔOD is shown in Fig. 2(a). At $t = 0$ ns the LIAD pulse hits the cell and increases the optical depth. The time resolution of the measurements is limited by the time jitter of the LIAD pulse (500 ps) and the single-photon counting module (350 ps).

First, we focus on a thicker part of the cell [$L = 6.24(7)$ μm], where we measure a time- and detuning-

resolved ΔOD map of the ^{85}Rb $F_g = 2$ transition of the D_2 line [Fig. 2(a)]. The transition is defined by the total angular quantum number F_g of the ground state g , while the total hyperfine splitting δ_{hfs} of the excited state cannot be resolved due to transient and Doppler broadening. The atoms moving in the laser propagation direction, originating from the entry facet of the cell, are probed at blue detunings $\delta > 0$. A second group of atoms, originating from the exit facet, is visible and probed at red detunings $\delta < 0$. The signal is higher for the atoms moving in the laser propagation direction. This asymmetry is not anticipated, but might originate from differences in the surface properties as it was observed in other experiments, i.e., depending on the coating [21]. We checked this hypothesis by rotating the cell by 180° , which led to a roughly inverted asymmetry. The darker region around zero detuning shows that fewer atoms with low z velocity are desorbed. In total, we measure two atom clouds moving toward the opposite cell walls. The high ΔOD value in the first nanoseconds is caused by a high atomic density and decreases over time. The ΔOD signal equilibrates to zero before the next LIAD pulse arrives. The dashed green lines indicate the time-of-flight curves, after which the atoms with a certain detuning hit the other cell wall according to $\text{TOF}(\delta) = Lk/|\delta|$, with $\delta = \mathbf{k} \cdot \mathbf{v} \pm \delta_{\text{hfs}}/2 = kv_z \pm \delta_{\text{hfs}}/2$, respecting the hyperfine splitting of the excited state. There, \mathbf{k} is the wave vector of the probe beam, which is parallel to the z axis, $k = |\mathbf{k}|$ is the wave number of the probe beam, \mathbf{v} is the velocity of the atom, and v_z is the z component of the velocity. We observe distinct signal wings beyond the respective time-of-flight curves indicating potential re-emission of

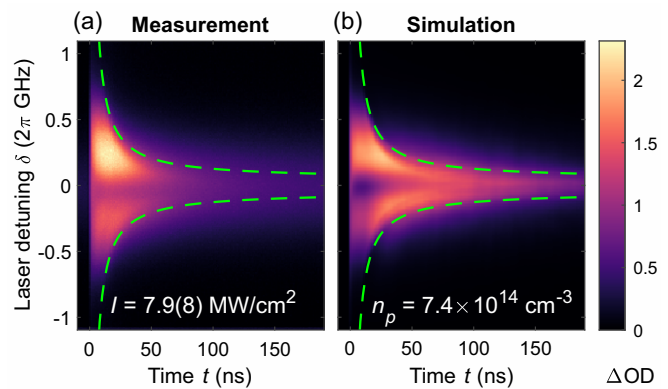


FIG. 2. (a) Measured ΔOD map of the ^{85}Rb $F_g = 2$ transition of the D_2 line. After the atoms, depending on their detuning (z velocity), hit the other cell wall the signal decreases. The $\text{TOF}(\delta)$ is shown with two dashed green lines. The intensity I is the peak intensity of the LIAD pulse. The cell thickness is $L = 6.24(7)$ μm and the reservoir temperature is $T_{\text{res}} \approx 140^\circ\text{C}$. (b) Simulated ΔOD map of desorbed atoms. The simulation parameters are adapted to the measurement. The $\text{TOF}(\delta)$ curves (dashed green lines) are plotted, too. The indicated n_p is the peak density at 2 ns.

atoms after arriving at the opposite cell wall.

Using this measurement as a reference, we develop a kinematic model and run a Monte Carlo simulation of atoms flying through a cell and interacting with the probe laser (see Supplemental Material [25]). The idea is to model the velocity distribution of desorbed atoms and to estimate the local density during the simulation.

In the model, the local and temporal desorption-rate scales linearly with the intensity of the LIAD pulse. For the velocity distribution we assume $f(v, \varphi, \theta) = [4/(\sqrt{\pi}a^3)v^2 \exp(-v^2/a^2)] \cos(\theta)$ with the parameter a and the speed $v = |\mathbf{v}|$. The azimuthal angle φ is uniformly distributed, while the polar angle θ is distributed according to the $\cos(\theta)$ -Knudsen law [31]. This simple distribution leads to a good qualitative agreement between measurement [Fig. 2(a)] and simulation [Fig. 2(b)]. We also assume that the atoms are desorbed only during the LIAD pulse and that there is no thermal desorption after the pulse, which is in good agreement with our measurement. Since no other mechanism (i.e., through natural- or transit-broadening, which are also included in the model) reproduces the signal wings beyond the time-of-flight curves (dashed green lines in Fig. 2), they might occur because of re-emissions from the surfaces after bombardment with the initial atom clouds. To get better agreement, an instant re-emission probability of 84% is included in the kinematic model.

The remaining discrepancies between measurement and simulation can originate from an inadequate velocity distribution model, intricate re-emission properties, additional decay mechanisms, the neglected Gaussian intensity distribution of the probe beam, and the use of the steady-state cross section of the atoms at all the times. Nevertheless, with the overall acceptable agreement between measurement and simulation we obtain a time- and z -dependent simulated local density, which shows that the desorbed atoms are initially in two flat, “pancakelike” clouds with an initial thickness well below the wavelength of the probe laser, rendering this into a 2D geometry (see Supplemental Material [25]).

To investigate high-density regimes, we use a thinner part of the cell, as the background optical depth and the detection limit of the single-photon counting module are limiting the measurement in the thicker part of the cell. We perform measurements at a cell thickness of $L = 0.78(2) \mu\text{m}$ at low and high atomic densities using the D_2 transition as shown in Figs. 3(a) and (b), respectively. Our measurements are in a regime where the total number of desorbed atoms per pulse monotonically increases with the peak intensity of the LIAD pulse (see Supplemental Material [25]). The low-density measurement corresponds to a peak intensity of $I = 2.6(3) \text{ MW cm}^{-2}$, while the high-density case corresponds to $I = 211(21) \text{ MW cm}^{-2}$.

There is a broadening and line shift of the D_2 hyperfine transitions present in Fig. 3(b), which we attribute to

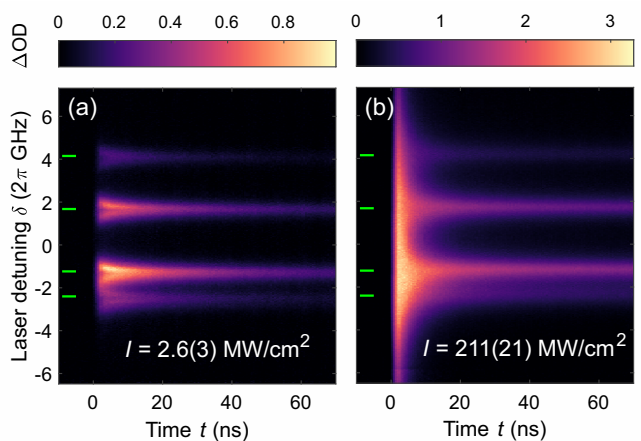


FIG. 3. Measurements of the time- and detuning-resolved ΔOD for low density (a) and high density (b) at the D_2 transition. There is a broadening and line shift of the spectrum in the first few nanoseconds for the high-density case. The measured broadening is mainly attributed to the density dependent self-broadening (Γ_{self}). The line shift occurs due to the dipole-dipole shift (Δ_{dd} , more visible in the slices presented in the Supplemental Material [25]). The four green markers indicate the ground state hyperfine splitting of the two isotopes of rubidium, respectively. The intensities I are the peak intensities of the LIAD pulse, the cell thickness is $L = 0.78(2) \mu\text{m}$, and the reservoir temperature is $T_{\text{res}} \approx 180^\circ\text{C}$.

density-dependent dipole-dipole interactions. The four peaks correspond to the ground state hyperfine splitting of the two isotopes of rubidium, contributing to the signal, while the hyperfine splitting of the excited state can not be resolved. The density-dependent self-broadening [3, 6] in the steady-state regime was predicted to be

$$\Gamma_{\text{self}} = \beta_i n = \frac{2}{3\hbar\epsilon_0} \sqrt{\frac{g_g}{g_e}} d_J^2 n, \quad (1)$$

where β_i is the self-broadening coefficient, i enumerates the D_1 or D_2 transition, \hbar is the reduced Planck constant, ϵ_0 is the vacuum permittivity, g_g and g_e are the multiplicities (depending on the quantum number J) of the ground and excited state respectively, d_J is the total reduced dipole matrix element, and n is the atomic density. In the high-density regime in Fig. 3(b) we observe a self-broadening of $\Gamma_{\text{self}} \approx 590\Gamma_0$ at $t = 2 \text{ ns}$, where $\Gamma_0 \approx 2\pi \times 6.07 \text{ MHz}$ [32] is the natural decay rate of the D_2 transition.

Similarly, we compare the line shift, observed in our measurements, to the steady-state dipole-dipole shift [5, 7], which was predicted to be

$$\Delta_{\text{dd}} = -|\Delta_{\text{LL}}| + \frac{3}{4} |\Delta_{\text{LL}}| \left(1 - \frac{\sin 2kL}{2kL} \right), \quad (2)$$

with Δ_{LL} being the Lorentz-Lorenz shift and L being the cloud thickness. This thickness dependency is a cavity-induced correction, also known as the collective Lamb

shift. The Lorentz-Lorenz shift [5, 7], in turn, is density-dependent and can be written as

$$\Delta_{\text{LL}} = -\frac{1}{3\hbar\epsilon_0}d_J^2n. \quad (3)$$

As our cell thickness is $L \approx \lambda$, the second term of the dipole-dipole shift has a significant effect on the line shift and reduces the dipole-dipole effect to $\Delta_{\text{dd}} \approx -\frac{1}{4}|\Delta_{\text{LL}}|$. In the high-density measurement in Fig. 3(b) this corresponds to a value of $\Delta_{\text{dd}} \approx -80\Gamma_0$ (redshift) at $t = 2$ ns. Additionally, we can observe that the transient density-dependent effects occur on a timescale of a few nanoseconds, which is faster than the natural lifetime of the D_2 transition (26.2 ns) [32].

To further investigate the dipole-dipole origin of the observed interaction, we compare the transient evolution of the self-broadening and line shift at the D_1 and D_2 transition of rubidium. We fit both measured data with a steady-state electric susceptibility model at each time

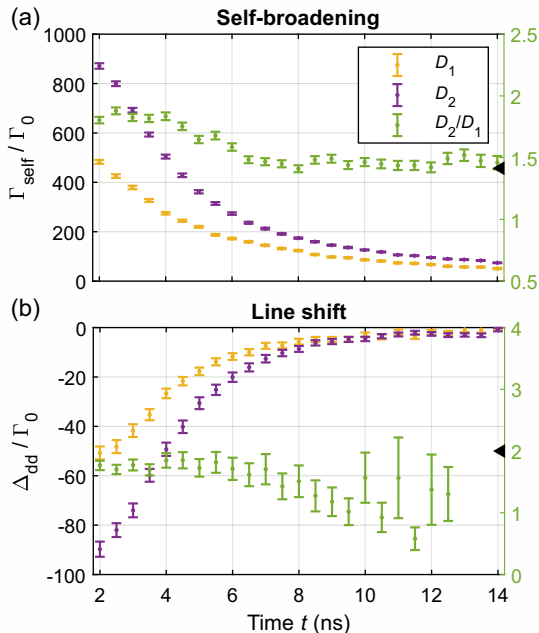


FIG. 4. (a) Time-dependent self-broadening Γ_{self} of the Rb spectra for the D_1 (yellow data) and D_2 (purple data) transition. The experiments are performed under identical conditions, except the probe laser wavelength. The ratio (green data) of the self-broadening of the two transitions approaches the theoretical steady-state ratio for large t (black triangle). Vertical error bars for $t < 8$ ns are likely underestimated due to a systematic effect, and horizontal precision is bandwidth limited by jitter. (b) Time-dependent line shift Δ_{dd} of the D_1 and D_2 transition. The ratio of the line shift, which is close to the theoretical value, has an increasing error for increasing time, and therefore the last three data points were omitted. The peak intensity of the LIAD pulse is $I = 317(32)$ MW cm $^{-2}$. The cell thickness is $L = 0.78(2)$ μm and the reservoir temperature is $T_{\text{res}} \approx 180$ $^{\circ}\text{C}$.

step, using the software ELECSUS [33]. The fits to the individual time-resolved spectra show a $< 6\%$ overall normalized root-mean-square deviation and result in the self-broadening and line shift shown in Figs. 4(a) and (b), respectively. Note that in the first 2 ns we cannot properly fit the data to this model, so we exclude these data points. The error bars represent the 1σ standard fit error (see Supplemental Material [25]). If we assume that the self-broadening and the line shift, according to the aforementioned steady-state equations, linearly depend on the density, we can calculate a peak density on the order of 10^{16} cm $^{-3}$ using Eqs. (1) and (2).

There is an apparent difference of the self-broadening and line shift between the two transitions of rubidium, which can be attributed to different transition dipole matrix elements d_J . While it is not possible to conclusively deduce any precise value for d_J from our data, we calculate ratios between the D_1 and D_2 broadening and shift for otherwise identical measurements, which are shown in Figs. 4(a) and (b) on the right vertical axis. These values approach the ratios $\sqrt{1/2}d_{J,D_2}^2/d_{J,D_1}^2$ and $d_{J,D_2}^2/d_{J,D_1}^2$ emerging from Eqs. (1) and (2), respectively, for large t as indicated by the black triangles. Deviations during the first ≈ 10 ns in the case of the self-broadening likely originate from limited accuracy of the fits with signal wings not captured with the scanned detuning range, asymmetries in the spectral profiles similar to what was reported in Ref. [8], or asymmetries from both hyperfine splitting and velocity distribution (see Fig. S4, Supplemental Material [25]). In contrast, the measured line shift is always much smaller than the scan range while almost vanishing for $t > 8$ ns such that the error bars are larger than the values themselves. Such systematic uncertainties are not properly captured by the standard errors as derived from the employed fitting algorithms.

In conclusion, we implemented a pulsed LIAD method to switch atom densities from 10^{14} cm $^{-3}$ to more than 10^{16} cm $^{-3}$ on a nanosecond timescale in a micrometer-sized cell. At high densities with $nk^{-3} \approx 100$ we are able to study the dipole-dipole induced self-broadening and Lorentz-Lorenz shift. Our measurements show that the interaction builds up faster than 2 ns, a timescale much shorter than the natural lifetime. The scaling between the D_1 and D_2 transition in the measurement supports the assumption that we observed dipolar effects in good agreement with the established theory. Overall, we do not see significant transient internal dynamics other than the one induced by the density change itself, since the motional dephasing is the fastest timescale equilibrating the shift and broadening of the many-body dynamics with dipolar interactions within ≈ 1 ns. With a better temporal resolution (e.g., with superconducting single-photon detectors) and shorter desorption pulses, it will be possible to study the behavior of the transient dipole-dipole interaction in the first 2 ns, a regime which was not accessible in this work. The switching of the atomic medium

by LIAD can be used with integrated photonic structures [34, 35], e.g., to realize large optical nonlinearities at a GHz bandwidth for switchable beam splitters, routers, and nonlinear quantum optics based on the excitation blockade.

The supporting data for this article are openly available from [36]. Additional data (e.g., raw data of the time tagger) are available on reasonable request.

The authors thank Artur Skljarow for extensive support during the preparation of the final version of this work. This work is supported by the Deutsche Forschungsgemeinschaft (DFG) via Grant No. LO 1657/7-1 under DFG SPP 1929 GiRyd. We also gratefully acknowledge financial support by the Baden-Württemberg Stiftung via Grant No. BWST_ISF2019-017 under the program Internationale Spitzenforschung. H.A. acknowledges the financial support from Eliteprogramm of Baden-Württemberg Stiftung, Graduiertenkolleg “Promovierte Experten für Photonische Quantentechnologien” via Grant No. GRK 2642/1, and Purdue University startup grant. C.S.A. acknowledges support from EPSRC Grant No. EP/R002061/1.

F.C., M.M., and F.M. contributed equally to this work.

* t.pfau@physik.uni-stuttgart.de

- [1] M. D. Lukin, M. Fleischhauer, R. Cote, L. M. Duan, D. Jaksch, J. I. Cirac, and P. Zoller, Dipole Blockade and Quantum Information Processing in Mesoscopic Atomic Ensembles, *Phys. Rev. Lett.* **87**, 037901 (2001).
- [2] L. A. Williamson, M. O. Borgh, and J. Ruostekoski, Superatom picture of collective nonclassical light emission and dipole blockade in atom arrays, *Phys. Rev. Lett.* **125**, 073602 (2020).
- [3] E. Lewis, Collisional relaxation of atomic excited states, line broadening and interatomic interactions, *Phys. Rep.* **58**, 1 (1980).
- [4] W. E. Lamb, Jr. and R. C. Retherford, Fine Structure of the Hydrogen Atom by a Microwave Method, *Phys. Rev.* **72**, 241 (1947).
- [5] R. Friedberg, S. Hartmann, and J. Manassah, Frequency shifts in emission and absorption by resonant systems of two-level atoms, *Phys. Rep.* **7**, 101 (1973).
- [6] L. Weller, R. J. Bettles, P. Siddons, C. S. Adams, and I. G. Hughes, Absolute absorption on the rubidium D_1 line including resonant dipole-dipole interactions, *J. Phys. B* **44**, 195006 (2011).
- [7] J. Keaveney, A. Sargsyan, U. Krohn, I. G. Hughes, D. Sarkisyan, and C. S. Adams, Cooperative Lamb Shift in an Atomic Vapor Layer of Nanometer Thickness, *Phys. Rev. Lett.* **108**, 173601 (2012).
- [8] T. Peyrot, Y. R. P. Sortais, A. Browaeys, A. Sargsyan, D. Sarkisyan, J. Keaveney, I. G. Hughes, and C. S. Adams, Collective Lamb Shift of a Nanoscale Atomic Vapor Layer within a Sapphire Cavity, *Phys. Rev. Lett.* **120**, 243401 (2018).
- [9] H. Dobbertin, R. Löw, and S. Scheel, Collective dipole-dipole interactions in planar nanocavities, *Phys. Rev. A* **102**, 031701(R) (2020).
- [10] V. Lorenz, X. Dai, H. Green, T. Asnicar, and S. Cundiff, High-density, high-temperature alkali vapor cell, *Rev. Sci. Instrum.* **79**, 123104 (2009).
- [11] A. Gozzini, F. Mango, J. H. Xu, G. Alzetta, F. Maccarrone, and R. A. Bernheim, Light-induced ejection of alkali atoms in polysiloxane coated cells, *Il Nuovo Cimento D* **15**, 709 (1993).
- [12] M. Meucci, E. Mariotti, P. Bicchi, C. Marinelli, and L. Moi, Light-Induced Atom Desorption, *Europhys. Lett.* **25**, 639 (1994).
- [13] E. B. Alexandrov, M. V. Balabas, D. Budker, D. English, D. F. Kimball, C.-H. Li, and V. V. Yashchuk, Light-induced desorption of alkali-metal atoms from paraffin coating, *Phys. Rev. A* **66**, 042903 (2002).
- [14] K. Rebilas and M. J. Kasprowicz, Reexamination of the theory of light-induced atomic desorption, *Phys. Rev. A* **79**, 042903 (2009).
- [15] P. A. Petrov, A. S. Pazgalev, M. A. Burkova, and T. A. Vartanyan, Photodesorption of rubidium atoms from a sapphire surface, *Opt. Spectrosc.* **123**, 574 (2017).
- [16] E. Talker, P. Arora, R. Zektzer, Y. Sebbag, M. Dikoptsev, and U. Levy, Light-induced atomic desorption in microfabricated vapor cells for demonstrating quantum optical applications, *Phys. Rev. Applied* **15**, L051001 (2021).
- [17] P. F. Griffin, K. J. Weatherill, and C. S. Adams, Fast switching of alkali atom dispensers using laser-induced heating, *Rev. Sci. Instrum.* **76**, 093102 (2005).
- [18] B. P. Anderson and M. A. Kasevich, Loading a vapor-cell magneto-optic trap using light-induced atom desorption, *Phys. Rev. A* **63**, 023404 (2001).
- [19] S. N. Atutov, R. Calabrese, V. Guidi, B. Mai, A. G. Rudavets, E. Scansani, L. Tomassetti, V. Biancalana, A. Burchianti, C. Marinelli, E. Mariotti, L. Moi, and S. Veronesi, Fast and efficient loading of a Rb magneto-optical trap using light-induced atomic desorption, *Phys. Rev. A* **67**, 053401 (2003).
- [20] C. Klempt, T. van Zoest, T. Henninger, O. Topic, E. Rasel, W. Ertmer, and J. Arlt, Ultraviolet light-induced atom desorption for large rubidium and potassium magneto-optical traps, *Phys. Rev. A* **73**, 013410 (2006).
- [21] S. Ghosh, A. R. Bhagwat, C. K. Renshaw, S. Goh, A. L. Gaeta, and B. J. Kirby, Low-light-level optical interactions with rubidium vapor in a photonic band-gap fiber, *Phys. Rev. Lett.* **97**, 023603 (2006).
- [22] A. D. Slepkov, A. R. Bhagwat, V. Venkataraman, P. Londero, and A. L. Gaeta, Generation of large alkali vapor densities inside bare hollow-core photonic band-gap fibers, *Opt. Express* **16**, 18976 (2008).
- [23] A. Burchianti, A. Bogi, C. Marinelli, C. Maibohm, E. Mariotti, and L. Moi, Reversible Light-Controlled Formation and Evaporation of Rubidium Clusters in Nanoporous Silica, *Phys. Rev. Lett.* **97**, 157404 (2006).
- [24] F. Ripka, H. Kübler, R. Löw, and T. Pfau, A room-temperature single-photon source based on strongly interacting Rydberg atoms, *Science* **362**, 446 (2018).
- [25] See Supplemental Material below for additional details on the experimental setup, evaluation and the kinematic model, which additionally includes Refs. [26–30].
- [26] N. Sekiguchi, T. Sato, K. Ishikawa, and A. Hatakeyama, Spectroscopic study of a diffusion-bonded sapphire cell for hot metal vapors, *Appl. Opt.* **57**, 52 (2017).

- [27] R. Loudon, *The Quantum Theory of Light* (Oxford University Press, Oxford, 2000).
- [28] D. A. Steck, Rubidium D Line Data, available online <http://steck.us/alkalidata> (revision 2.2.2, 9 July 2021).
- [29] M. Knudsen, *The Kinetic Theory of Gases. Some Modern Aspects* (Methuen & Co., London, 1934).
- [30] N. Šibalić, J. D. Pritchard, C. S. Adams, and K. J. Weatherill, ARC: An open-source library for calculating properties of alkali Rydberg atoms, *Comput. Phys. Commun.* **220**, 319 (2017).
- [31] G. Comsa and R. David, Dynamical parameters of desorbing molecules, *Surf. Sci. Rep.* **5**, 145 (1985).
- [32] U. Volz and H. Schmoranzner, Precision lifetime measurements on alkali atoms and on helium by beam-gas-laser spectroscopy, *Phys. Scr.* **T65**, 48 (1996).
- [33] M. A. Zentile, J. Keaveney, L. Weller, D. J. Whiting, C. S. Adams, and I. G. Hughes, ElecSus: A program to calculate the electric susceptibility of an atomic ensemble, *Comput. Phys. Commun.* **189**, 162 (2015).
- [34] R. Ritter, N. Gruhler, H. Dobbertin, H. Kübler, S. Scheel, W. Pernice, T. Pfau, and R. Löw, Coupling Thermal Atomic Vapor to Slot Waveguides, *Phys. Rev. X* **8**, 021032 (2018).
- [35] H. Alaeian, R. Ritter, M. Basic, R. Löw, and T. Pfau, Cavity QED based on room temperature atoms interacting with a photonic crystal cavity: a feasibility study, *Appl. Phys. B* **126**, 25 (2020).
- [36] F. Christaller, M. Mäusezahl, F. Mounstilis, A. Belz, H. Kübler, H. Alaeian, C. S. Adams, R. Löw, and T. Pfau, Data for “Transient Density-Induced Dipolar Interactions in a Thin Vapor Cell”, Zenodo [10.5281/zenodo.6411102](https://doi.org/10.5281/zenodo.6411102) (2022).

**SUPPLEMENTAL MATERIAL FOR
“TRANSIENT DENSITY-INDUCED DIPOLAR INTERACTIONS IN A THIN VAPOR CELL”**

CONTENTS

I. Overview and definitions	7
II. Experimental setup	7
III. Atomic density for increasing LIAD intensity	8
IV. Kinematic model and simulation	9
V. ELECSUS fitting procedure	10
VI. Pulsed LIAD probed at 420 nm	12

I. OVERVIEW AND DEFINITIONS

This Supplemental Material roughly follows the structure of the manuscript, providing additional information alongside. In section II the experimental prerequisites to perform our LIAD measurements are detailed and the principle data analysis procedure is introduced. Section III elaborates our findings about the behavior of the desorption process when the LIAD pulse intensity is increased. This forms a necessary foundation for the development of our kinematic model discussed in section IV, as the latter makes certain assumptions about the number of atoms which get desorbed during each pulse. Section V frames the discussion of Fig. 4 in the manuscript by showing how the individual data points were processed and compared. Section VI concludes this work by highlighting another approach pursued to deepen the understanding of the dipolar origin of the observed effects. This Supplemental Material and the manuscript share consistent definitions of all introduced symbols. All frequencies are given as angular frequencies, such that detunings Δ and decay-induced linewidths Γ all appear on the same scale without additional conversion factors. We define the laser detuning δ as the actively adjusted laser frequency ω_l compared to a resonant atomic transition frequency ω_a like $\delta = \omega_l - \omega_a$. An additional detuning occurs due to the velocity \mathbf{v} of the atoms as we deal with a thermal gas. Moreover, there are additional sources of line shifts such as dipole-dipole effects Δ_{dd} which are included in the perceived detuning Δ_{atom} of an atom given by

$$\Delta_{atom} = \omega_a - \omega_l + \mathbf{k} \cdot \mathbf{v} + \Delta_{dd} \quad (\text{S4})$$

$$= -\delta + \mathbf{k} \cdot \mathbf{v} + \Delta_{dd} . \quad (\text{S5})$$

The time-of-flight TOF(δ) curves in Fig. 2 in the manuscript and Fig. S3, which are given in the maps as an guide to the eye, can be understood as the time-of-flight solution of Eq. (S5) for an atom with zero perceived

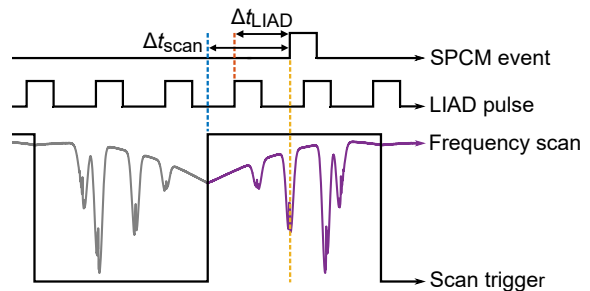


FIG. S1. Trigger sequence during the detection of a photon. The time tagger module receives electrical triggers from three different sources: The SPCM, the LIAD pulse generator and the scan ramp generator of the probe laser. Each event in the SPCM channel (each photon) is referenced to the most recent LIAD pulse trigger and scan trigger. The resulting time differences Δt_{LIAD} directly indicate the temporal position of the observed photon with respect to the LIAD pulse. The time differences Δt_{scan} can be converted to a temporary laser frequency by comparing the scan trigger sequence to an absolute frequency reference indicated by an atomic saturation spectroscopy signal (purple curve).

detuning $\Delta_{atom} = 0$ and no additional shifts $\Delta_{dd} = 0$ (i.e. resonant interaction under Doppler effect with otherwise negligible linewidth) when traveling across the cell.

II. EXPERIMENTAL SETUP

In order to observe a time- and detuning-resolved LIAD process and the consequent velocity and density map, each detected photon must be assigned to a time t after the LIAD pulse and a detuning δ . We use a single-photon counting module (SPCM-AQRH-10-FC from Excelitas), which has a specified single photon timing resolution of 350 ps. Its electrical triggers are temporally digitized by a time tagger module (Time Tagger 20 from Swabian Instruments) with a specified RMS (root-mean-square) jitter of 34 ps. This produces an absolute timestamp $t_{SPCM,k}$ for each observed photon ($k \in \mathbb{N}$). The LIAD laser pulses are electrically triggered from a pulse generator (Bergmann BME_SG08p) at 50 kHz repetition rate with a specified delay resolution of 25 ps and an output to output RMS jitter of less than 50 ps. These electrical pulses are fed into a Q-switched 532 nm laser (BrightSolutions WedgeHF 532) with an experimentally determined pulse-to-pulse jitter of less than 500 ps. We use an additional synchronized output from the pulse generator as temporal reference for the laser pulses generating additional timestamps $t_{LIAD,\ell}$, ($\ell \in \mathbb{N}$). At the same time, a Littrow-configuration, external-cavity diode laser (Toptica DL Pro) is continuously

frequency-scanned over the ranges shown in the figures of the manuscript at a rate of 11 Hz. This ensures that the effective detuning δ is quasi constant during each individual LIAD pulse and the transient regime, which is on the order of less than a microsecond. It additionally provides a large number of LIAD pulses for each detuning in every dataset spanning over an integration time in the order of one day. The scan ramp triggers are fed into the time tagger module and generate a series of timestamps $t_{\text{scan},m}$, ($m \in \mathbb{N}$). This overall trigger sequence for a single photon detection is schematically depicted in Fig. S1. During analysis, time differences

$$\Delta t_{\text{LIAD},k} = t_{\text{SPCM},k} - t_{\text{LIAD},\ell} \quad \text{and} \quad (\text{S6})$$

$$\Delta t_{\text{scan},k} = t_{\text{SPCM},k} - t_{\text{scan},m} \quad (\text{S7})$$

are calculated, such that each SPCM timestamp gets assigned to the most recent LIAD and scan trigger. The value $\Delta t_{\text{LIAD},k}$ reflects the timing with respect to the desorption pulse. The different electrical and optical propagation times are corrected by observing LIAD pulses directly on the same SPCM and subtracting their average peak pulse position to obtain time differences on a time axis t , which is plotted in all figures in this work. Similarly, $\Delta t_{\text{scan},k}$ relates to the temporary probe laser frequency $\omega_{l,k}$ by a certain function $\omega_l(\Delta t_{\text{scan}}, t_{\text{SPCM}})$. The direct dependency on the absolute time t_{SPCM} indicates that laser frequency drifts must be corrected. This is achieved by calibrating to an ultra low expansion (ULE) cavity captured continuously on a digital oscilloscope. The ULE cavity has a free spectral range of $2\pi \times 1.5$ GHz and an overall negligible drift. The absolute frequency with respect to the atomic transitions can be determined by additionally observing a saturated rubidium spectrum on the same oscilloscope. All values δ are given with respect to the center-of-mass of the shown transition(s). Note that the function $\omega_l(\Delta t_{\text{scan}}, t_{\text{SPCM}})$ is calculated stepwise to reflect the different behavior during the rising and falling scan ramp. We estimate an overall statistical uncertainty for δ of less than $2\pi \times 10$ MHz, mainly limited by fluctuations of the scan rate during each scan ramp not captured by the $2\pi \times 1.5$ GHz ULE cavity.

The plotted maps with respect to t and δ are calculated by binning relevant pairs $(t, \delta)_k$ into a 2D histogram. A bin width of $2\pi \times 10$ MHz to $2\pi \times 50$ MHz for δ and 500 ps for t is used throughout this work. The bin width of t is thus chosen on the same order of magnitude as the time jitter limiting the overall measurement. The binning of the probe laser detuning can be chosen more arbitrarily to suppress the noise. For the displayed data we use a bin-width larger than the free-running linewidth of the probe laser ($\nu \approx 2\pi \times 800$ kHz).

From the various measurements shown in the manuscript and the experience with our setup, we can state, that the observations due to the LIAD effect are repeatable after

months and years. Yet we have to mention, that during measurements with high LIAD pulse intensity, the cell is locally modified. This modification manifests itself as a decreased transmission or visibly brown spot, which, depending on the total exposure, can be either temporary and healed by uniform heating or stay permanently. We attribute this behavior to an alteration of the sapphire coating after bombardment with rubidium atoms. We could not observe such a change in transmission in a similar cell filled with air under otherwise identical conditions. We also note that a similar discoloration and loss of transmission is a well-known effect for cells filled with alkali vapor at elevated temperatures [26]. It could be possible that the LIAD effect and velocity distribution locally produce a similar phenomenon even at lower temperatures. To minimize the impact of such effects on our measurements, we monitor the probe transmission and regularly move the cell to a spot with the same cell thickness to continue the measurement once a noticeable transmission loss is observed. Thereby, we gain reproducible results over multiple measurement runs.

III. ATOMIC DENSITY FOR INCREASING LIAD INTENSITY

In this work we present the change of the optical depth ΔOD as an indicator for the temporally-controlled, additional atomic density (or equivalently the number of desorbed atoms) compared to a vapor cell homogeneously heated to a certain background temperature. It is plausible to assume that for LIAD pulses of fixed duration, the number of desorbed atoms increases with increasing LIAD pulse peak intensity I , since the total energy introduced into the system increases. While we could not deduce a simple relationship between the parameters for a velocity distribution model (see section IV) and the LIAD pulse parameters, we still observe well-defined relationships between I and key features of the corresponding ΔOD maps.

One such feature is the peak optical depth value reached on resonance, $\Delta\text{OD}_{\text{peak}}$, as an indicator for the total number of atoms desorbed during the process. Fig. S2(a) shows that these values monotonically increase for both the D_1 and D_2 transition with increasing I . As the attainable atomic density is independent of the probe wavelength and therefore roughly identical in both cases, the ratio between the individual $\Delta\text{OD}_{\text{peak}}$ values for both transitions should be proportional to their resonant scattering cross section σ_0 , which in turn can be related to the transition dipole moment d as $\sigma_0 \propto |d|^2$ [27]. This assumes steady-state behavior and is therefore not perfectly reproduced in our case. A much stronger absorption of light at the D_2 transition however is visible, which is expected given the transition dipole moment squared is larger by factor of roughly 2 compared to the D_1 tran-

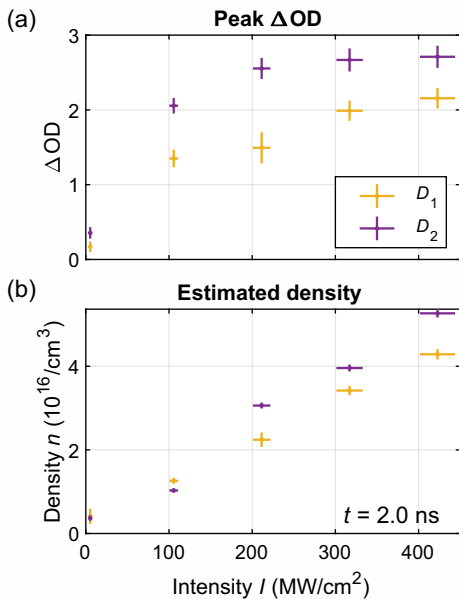


FIG. S2. (a) Measured values of ΔOD_{peak} for various LIAD pulse peak intensities. All other parameters of the system are kept identical and comparable to the settings discussed in Fig. 3 in the manuscript. (b) Density $n(t = 2 \text{ ns})$ calculated from the fitted broadening and shift values using Eqs. (1) and (2) from the manuscript.

sition [28]. The displayed horizontal error bars in Fig. S2 show the 10% standard deviation of the LIAD peak intensity due to power fluctuations. The vertical error bar of the ΔOD is determined via error propagation from the statistical uncertainty of the photon counts N_{photon} , which is given by $\Delta N_{\text{photon}} = \sqrt{N_{\text{photon}}}$. The highest ΔOD_{peak} shown in Fig. S2(a) is at the limit of what can be detected with our setup due to the low number of events detected by the SPCM modules compared to the background noise of the system (dark count rate R_{dark}). From the datasheet provided by the manufacturer and reference measurements, we estimate at $R_{\text{dark}} \approx 1.5 \times 10^3 \text{ s}^{-1}$ with an average count rate $R_{\text{avg}} \approx 1 \times 10^6 \text{ s}^{-1}$, an overall $\text{OD}_{\text{peak}} = \ln(R_{\text{avg}}/R_{\text{dark}}) \approx 6.5$ might just be accessible. This also includes the optical depth contribution of the thermal background vapor, which was less than 0.5 for the largest cell thicknesses presented in this work ($L = 6.24 \mu\text{m}$). The observed behavior ΔOD_{peak} with I could therefore be attributed to statistical limits of the SPCM in addition to the density broadening and the unknown microscopic behavior of the cell wall's material. The latter include temporary (i.e. debris, accumulation of rubidium atoms) and permanent (i.e. cell damage) modifications for prolonged measurement cycles at one spot of the wedge-shaped cell. The relation between a growing ΔOD_{peak} and the underlying atomic density n_{peak} becomes nonlinear at high densities due to the atomic interactions and cannot be calculated directly without precise knowledge about the

density broadening effect and the actual density- and velocity distribution. The actual peak density n_{peak} might therefore show e.g. a linear trend with I , while the growth of ΔOD_{peak} appears to saturate [Fig. S2(a) data points at larger I]. The manuscript mentions a possible approach using steady-state derivations starting from the fitted broadening and shift. There, the presented order of magnitude of the density is calculated using Eqs. (1) and (2) from the manuscript. As the broadening and the shift lead to almost the same density values, we can calculate the average density from these two values and plot the estimated density at $t = 2 \text{ ns}$ for different LIAD peak intensities, as shown in Fig. S2(b). There, we observe an almost linear behavior between the LIAD peak intensity and the estimated density from both the D_1 and D_2 transition. The uncertainties of the estimated density result from the susceptibility fits done with ELECSUS. Note, that we apply a steady-state model to determine these density values and we have no other independent way to measure the transient density (see section V).

IV. KINEMATIC MODEL AND SIMULATION

This section describes how the kinematic model and the Monte Carlo simulation are set up to generate the optical depth map numerically [Fig. 2(b) in the manuscript]. As a first step, we pick atoms on one of the two inner cell walls ($z = 0$ or $z = L$, with the cell thickness L). The x and y position of the atoms are distributed normally, where the width of the distribution is given by the waist radius of the LIAD beam $w_{\text{LIAD}} = 13.7 \mu\text{m}$ (atoms are only desorbed where the LIAD beam hits the cell). We choose a velocity distribution of the form $f(v, \varphi, \theta) = [4/(\sqrt{\pi}a^3)v^2 \exp(-v^2/a^2)] \cos(\theta)$ with the parameter a , adjusted to agree with the measurement. As for the angular part of this distribution, the azimuthal angle φ is uniformly distributed and the polar angle θ is distributed according to the $\cos(\theta)$ -Knudsen law [29, 31]. The desorption time of the atoms is defined by the temporal shape of the LIAD pulse. This pulse has a shape similar to the Blackman window with a length of 1.1 ns (FWHM). The asymmetry of the measurement between the two atom clouds moving in or against the laser propagation direction (atoms with positive and negative detuning, respectively) is captured via a ratio variable r . This ratio r is defined as the total number of atoms with negative detuning over the total number of atoms with positive detuning. After each atom traveled through the cell and hit the opposite wall, it can lead to a re-emission of another atom from the cell wall with a certain probability p_r and with a new velocity (v : Maxwell-Boltzmann; φ, θ : uniform). Only atoms which enter the cylindrical probe beam with a radius of $w_{\text{probe}} = 2.0 \mu\text{m}$ are considered. The actual transversal Gaussian profile of the probe beam is therefore approximated by a tophat pro-

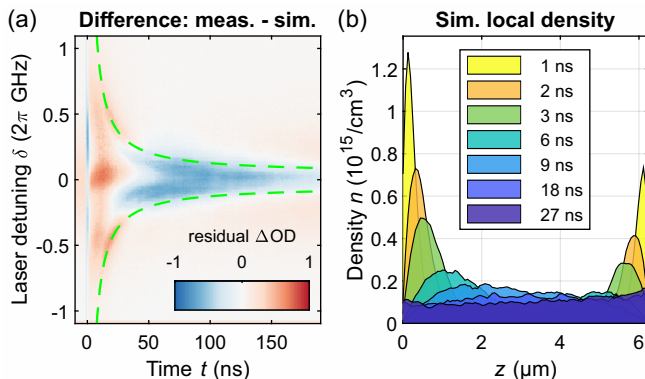


FIG. S3. (a) Difference between measured and simulated ΔOD map, which are shown in Fig. 2 in the manuscript. The residual ΔOD value indicates where the simulation under- or overestimates the measurement. The $\text{TOF}(\delta)$ is shown with two dashed green lines. (b) Simulated local density in the $6.24\ \mu\text{m}$ thick cell. The high density at both cell walls ($z = 0\ \mu\text{m}$ and $z = 6.24\ \mu\text{m}$) is decreasing with increasing time after the LIAD pulse. After $t \approx 18\ \text{ns}$ the atoms are uniformly distributed along the z axis of the cell.

file to simplify the decision whether a particle is currently inside the probe beam. This is valid due to its small diameter compared to the LIAD beam and allows for an ad-hoc implementation of transit-time broadening effects without the need to solve the time-dependent optical Bloch equations for each atom. The simulation parameters for Fig. 2(b) in the manuscript are displayed in Table S1. These values were simultaneously optimized using a supervised pattern search algorithm by minimizing the root-mean-square (RMS) value of the residual ΔOD map. This map is the difference between the measurement and the simulation, shown in Fig. S3(a). From the parameter a one can estimate a temperature corresponding to the desorbed atoms, which is $T_{\text{sim}} \approx 100^\circ\text{C}$. The second step is the calculation of the time- and z -dependent local density $n(t, z)$ of the atoms. The z axis with the cell thickness L is sliced into N_z slices. For each simulation time step and each slice, the number of atoms in a slice is counted and divided by the slice volume. For large numbers of atoms it is possible to only simulate a fraction of all atoms and rescale this value accordingly. This gives a time- and z -dependent estimation of the density in the cell, shown in Fig. S3(b).

As a third step, the scattering cross section for the simulated time steps and laser detunings are calculated using

TABLE S1. Parameters used in the simulation to reproduce the measurement. The values are adjusted to minimize the RMS of the residual ΔOD map, shown in Fig. S3(a).

variable	a	r	p_r
value	$271\ \text{m s}^{-1}$	0.6	0.84

a steady-state model as an approximation. For each time step t , laser detuning δ and atom i the resulting detuning is determined as $\Delta_{\text{atom}} = -\delta + kv_{z,i} + \Delta_{\text{dd},i}$, where $k = 2\pi/\lambda$ is the laser wave number and Δ_{dd} is the additional dipole-dipole line shift, which depends on the local density. In addition to the natural decay rate Γ_0 , we also include the transit broadening $1/\tau_{\text{tt}}$ for each individual atom to model the finite probe size effect. After including the density-dependent self-broadening Γ_{self} , the total broadening reads as $\Gamma = \Gamma_0 + 1/\tau_{\text{tt},i} + \Gamma_{\text{self},i}$.

The steady-state scattering cross section is defined as [28]

$$\sigma(\Delta_{\text{atom}}, I) = \frac{\sigma_0}{1 + 4(\Delta_{\text{atom}}/\Gamma_0)^2 + (I/I_{\text{sat}})}, \quad (\text{S8})$$

where σ_0 is the resonant scattering cross section, defined as [28]

$$\sigma_0 = \frac{\hbar\omega_a\Gamma_0}{2I_{\text{sat}}}. \quad (\text{S9})$$

With the additional broadening effects the scattering cross section has to be normalized with Γ_0/Γ . As we are in the weak probe regime with $I_{\text{probe}} < I_{\text{sat}}$, the scattering cross section can be written as

$$\sigma(\Delta_{\text{atom}}, \Gamma) = \frac{\Gamma_0}{\Gamma} \frac{\sigma_0}{1 + 4(\Delta_{\text{atom}}/\Gamma)^2}. \quad (\text{S10})$$

To capture the dipolar dynamics of the atom-probe interaction, we use time-dependent Δ_{dd} and Γ_{self} values due to the time- and z -dependent atomic density [see Eqs. (1) and (2) in the manuscript]. The scattering cross sections are accumulated and normalized for all simulated atoms within the probe region for each time step, laser detuning and z slice as $\sigma(t, \delta, z)$. This can be understood as the average cross section $\sigma(\delta)$ contributed by an atom found at time t at location z .

The last step is the conversion of the calculated density $n(t, z)$ and scattering cross section $\sigma(t, \delta, z)$ to an optical depth according to the Beer-Lambert law. This correctly captures shadowing effects among atoms if the density in each z slice is low compared to its thickness (s.t. $n\sigma L/N_z \ll 1$) and can be formulated for z -dependent n and σ . Since we only simulate the desorbed atoms without any background gas, the calculated change of the optical depth is

$$\Delta\text{OD}(t, \delta) = \int_0^L \sigma(t, \delta, z)n(t, z)dz. \quad (\text{S11})$$

V. ELECSUS FITTING PROCEDURE

Here we show some exemplary electric susceptibility fits done with ELECSUS [33]. The data points were weighted according to their inverse uncertainties shown

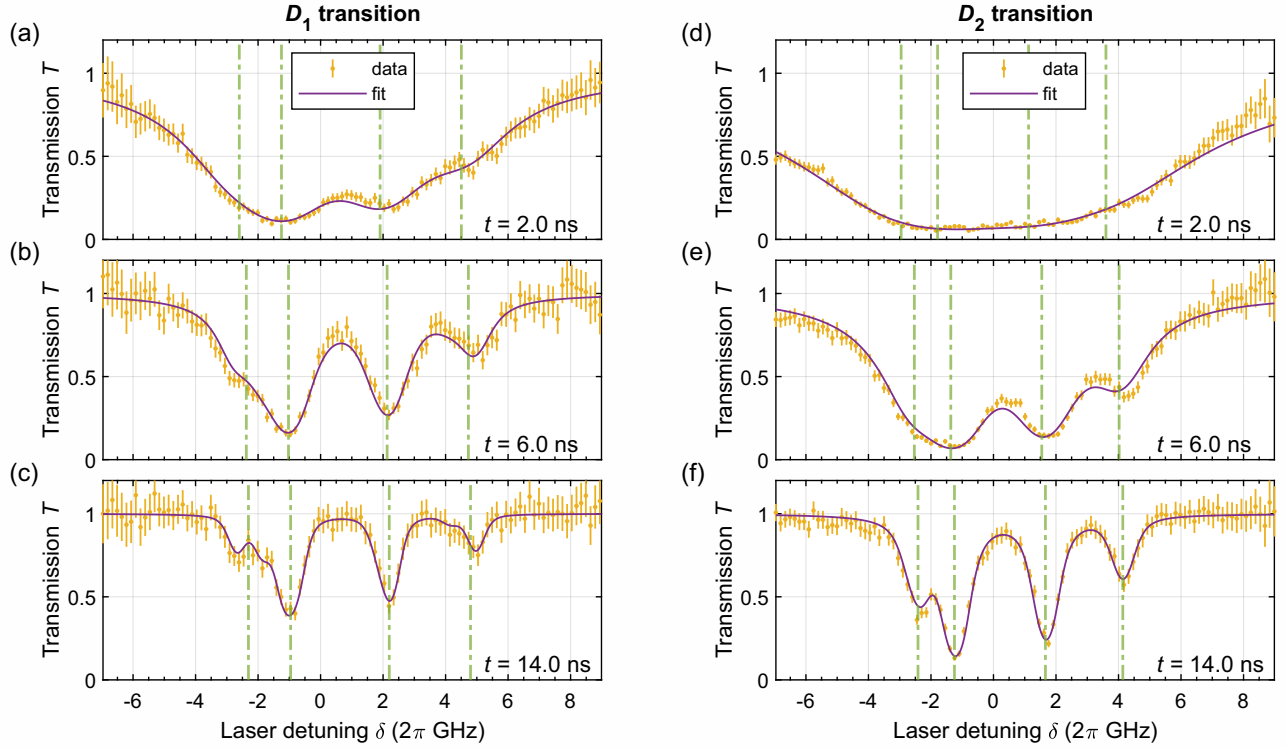


FIG. S4. Fits of an electric susceptibility model to the measured data of the D_1 transition in (a,b,c) and D_2 transition in (d,e,f). The data points (yellow, only every third data point shown) and the fit (purple) are in good agreement. The fits are performed for every time t in steps of the time binning. Exemplary data are the times $t = 2$ ns in (a,d), $t = 8$ ns in (b,e), and $t = 14$ ns in (c,f). For the traceability of the changing line shift over time, we mark the shifted frequencies of the two ground state hyperfine splittings of the two rubidium isotopes with four green vertical lines. The cell thickness is $L = 0.78(2)$ μm , the peak intensity of the LIAD pulse is $I = 317(32)$ MW cm^{-2} , and the reservoir temperature is $T_{\text{res}} \approx 180$ $^\circ\text{C}$.

in Fig. S4. The error bars on the wings of the spectrum are larger due to a filter etalon in the setup, reducing the number of photon counts N_{photon} and thereby increasing the statistical uncertainty $\Delta N_{\text{photon}} = \sqrt{N_{\text{photon}}}$. We start fitting from larger times t , with negligible interaction, to shorter times, showing strong interaction effects, using the results from the previous fit as initial parameters for the next fit. Note that the ELECSUS internal treatment of the self-broadening is manually switched off to get the full information of the broadening from the fits. We also set the Doppler temperature to $T_{\text{Doppler}} = 0$ $^\circ\text{C}$, as we mainly want a Lorentzian profile, which is in first approximation justified to capture the self-broadening ($\Gamma_{\text{self}} > \Gamma_{\text{Doppler}}$). The free fit parameters for our ELECSUS fits are the width of the Lorentzian profile (Γ_{buf} , normally used for a buffer gas broadening), the line shift and the temperature of the cell T_{cell} , which is used to calculate a temperature-dependent atomic density. Note, that this intrinsic temperature-dependent density in ELECSUS is not a useful quantity in our anisotropic system and therefore not considered in this work. In our system the velocity of the atoms has a certain direction, where a possible velocity distribution is discussed in our kinematic model (see also Section IV).

The ELECSUS software calculates the 1σ standard error of the fitted variables. These standard errors are plotted as vertical error bars in Fig. 4 in the manuscript and in Fig. S5. There are no horizontal error bars shown in both these figures, as they originate from histogram binning. In this sense, the horizontal precision is limited by the bin width which is motivated by the the total temporal precision $\Delta t_{\text{total}} = 850$ ps of each captured event. This Δt_{total} is the sum of the LIAD pulse-to-pulse jitter and the time resolution of the SPCM, which limit the bandwidth of the measurement. The goodness of each fit is evaluated by calculating the normalized root-mean-square deviation NRMSD as given in the manuscript, which is calculated from the root-mean-square deviation $\text{RMSD} = N^{-1} \sqrt{\sum_{i=1}^N (T_i - \hat{T}_i)^2}$ between the measured transmission points T_i and the fitted transmission value \hat{T}_i . These are then normalized using the minimum and maximum transmission values $T_{\text{min}} = 0, T_{\text{max}} = 1$ as $\text{NRMSD} = \text{RMSD} / (T_{\text{max}} - T_{\text{min}})$. The obtained values are similar for both probe transitions and typically at $\text{NRMSD} \approx 5\%$.

The electric susceptibility model is a steady-state solution of the atom-light interaction. As mentioned in the manuscript, we cannot properly fit the data points in the

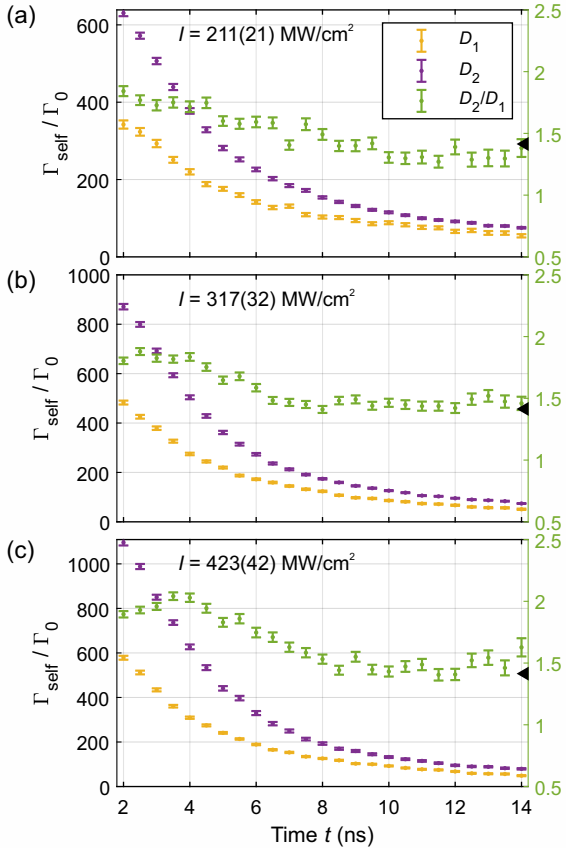


FIG. S5. Self-broadening of the D_1 (yellow) and D_2 (purple) transition over time for three different LIAD intensities I . Additionally, the ratio D_2/D_1 (green) is plotted, which is approaching the theoretical steady-state ratio (black triangle). For high intensities, e.g. in (c), the broadening of the D_2 transition is overestimated during the fit (see also Fig. S4), which is one reason for the deviation of the ratio from the theoretical value in the first ≈ 10 ns.

first 2 ns. Initially the broadening is large and the signals' wings are not properly captured with $\approx 2\pi \times 16$ GHz scan range in our experiment. Also the LIAD pulse, which is present until $t \approx 1.5$ ns, distorts the measured data. There are several effects which could systematically distort the quality of the fit results or render the model unsuitable for later times t (ordered by the hypothesized contribution from strongest to lowest according to the authors): A non-isotropic velocity distribution as produced by the LIAD pulse, geometry-dependent effects like the collective Lamb shift, mathematical artifacts due to a clipped detuning range, asymmetries from different relative hyperfine transition strengths and dipole moments, asymmetric line shapes caused by any other effect (e.g. surface potentials), multi-particle interactions, differences in the experimental configuration between both transitions, and temporally transient dipolar effects. The ratio between the line shifts can be properly recovered from the fits for $t < 7$ ns even if the wings are not

fully captured, as the the dipole-dipole shift is smaller than the self-broadening and can be measured as an absolute offset instead of a line width. For very large times, corresponding to low densities, the ratio between the vanishing shifts on the D_1 and D_2 transition will be very susceptible to any residual offset. In this region, which occurs at different times for self-broadening and line shift due to their different absolute values, we observe varying and unstable behavior. We suspect that a combination of all these effects causes deviations from the theoretical ratios between the D_1 and D_2 transition as reported in Fig. 4 in the manuscript.

While the self-broadening is directly visible in Fig. S4 for exemplary times, we also show the fitted line shift by drawing the frequencies of the two ground state hyperfine splittings of the two rubidium isotopes, to emphasize the changing line shift over time. The figure also highlights that artifacts due to a clipped laser detuning range would impact the D_1 transition less (or at different times) than the D_2 transition. This idea is supported by the reduced variation in the D_2/D_1 ratio in Fig. S5(a), which indeed has the lowest overall density and broadening.

To underline our observation of the transient density-dependent dipolar interactions, we show the time evolution of the self-broadening for two additional LIAD intensities in Fig. S5. With increasing intensity, the density is also increasing, leading to a larger self-broadening. The ratio of D_2/D_1 shows a similar behavior for all intensities.

VI. PULSED LIAD PROBED AT 420 nm

The experiments in the manuscript were performed using probe lasers at the D_1 and D_2 ground state transitions, with relatively large transition dipole moments.

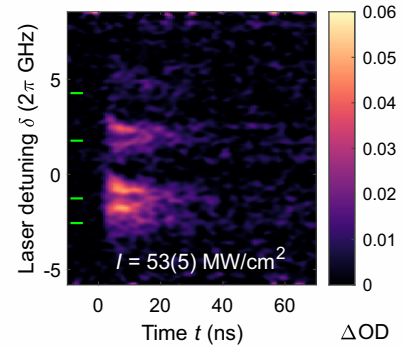


FIG. S6. Measured ΔOD map on the $5S_{1/2} \rightarrow 6P_{1/2}$ transition at a cell thickness of $2.34(4)$ μm and a reservoir temperature of $T_{\text{res}} \approx 230^\circ\text{C}$. The four green markers indicate the ground state hyperfine splitting of the two isotopes of rubidium, respectively. Note, that the image has been filtered using a Gaussian filter to reduce the overall noise in the data. The intensity I is the peak intensity of the LIAD pulse.

This, however, induces limits considering the accessible density regimes before broadening effects become larger than the captured frequency range as discussed above. It can be overcome by probing on a transition with a lower transition dipole moment.

We therefore modified our measurement setup to include a 421.6 nm laser probing the $5S_{1/2} \rightarrow 6P_{1/2}$ transition, where the squared transition dipole moments are reduced by roughly two orders of magnitude [30]. The measured data for total integration times similar to the previously discussed cases exhibits a much noisier signal and lower ΔOD , which is expected due to the much weaker transition dipole moment. Consequently, the resulting map

shown in Fig. S6 could only be captured for relatively strong LIAD pulses, a thicker part of the cell, and a higher reservoir and cell temperature. Important features discussed in the manuscript are reproduced. Both signals representing atoms moving towards and away from the laser are visible and exhibit the same asymmetry towards atoms moving in propagation direction of the LIAD laser. We were not able to measure a line shift or broadening which is attributed to the significantly weaker transition dipole moment. This further supports the conclusion that the observed effects in the manuscript indeed have a dipolar origin.

F.C., M.M., and F.M. contributed equally to this work.